Title: Turbulence effects on cellular burning structures in lean premixed hydrogen flames

Authors: Marc Day[a], John Bell[a], Peer-Timo Bremer[b], Valerio Pascucci[c], Vince Beckner[a], Michael Lijewski[a]

[a]*Lawrence Berkeley National Laboratory*

[b]*Lawrence Livermore National Laboratory*

[a]*Scientific Computing and Imaging Institute, University of Utah*

Article Type: Full-length

Corr. Author: Marc Day

Mailstop 50A-1148

One Cyclotron Road

Berkeley, CA 94553 USA

(510) 486-5076 (tel)

(510) 486-6900 (fax)

MSDay@lbl.gov

Shortened Title: Turbulent premixed cellular hydrogen flames

Turbulence effects on cellular burning structures in lean premixed hydrogen flames

Marc Day [a,*], John Bell [a], Peer-Timo Bremer [b],
Valerio Pascucci [c], Vince Beckner [a] and Michael Lijewski [a]

[a]*Lawrence Berkeley National Laboratory,*
Mailstop 50A-1148, One Cyclotron Road, Berkeley, CA 94720, USA.

[b]*Lawrence Livermore National Laboratory,*
Box 808, L-560, Livermore, CA 94551-0808, USA.

[c]*Scientific Computing and Imaging Institute, University of Utah*
72 S Central Campus Drive, 3750 WEB, Salt Lake City, UT 84112, USA.

Abstract

We present numerical simulations of lean hydrogen flames interacting with turbulence. The simulations are performed in an idealized setting using an adaptive low Mach number model with a numerical feedback control algorithm to stabilize the flame. At the conditions considered here, hydrogen flames are thermodiffusively unstable, and burn in cellular structures. For that reason, we consider two levels of turbulence intensity and a case without turbulence whose dynamics is driven by the natural flame instability. An overview of the flame structure shows that the burning in the cellular structures is quite intense, with the burning patches separated by regions in which the flame is effectively extinguished. We explore the geometry of the flame surface in detail, quantifying the mean and Gaussian curvature distributions and the distribution of the cell sizes. We next characterize the local flame speed to quantify the effect of flame intensification on local propagation speed. We then introduce several diagnostics aimed at quantifying both the level of intensification and diffusive mechanisms that lead to the intensification.

Key words: Turbulent, Premixed, Hydrogen, Simulation, Morse theory
PACS:

* Corresponding author.
  Email address: MSDay@lbl.gov (Marc Day).
  URL: http://seesar.lbl.gov/ccse/ (Marc Day).

1 Introduction

There has been considerable recent interest in the development of premixed burners capable of stably burning hydrogen at lean conditions. Operating at fuel-lean conditions minimizes combustion exhaust gas temperatures, which in turn reduces the formation of nitrogen-based emissions downstream of the flame. However, lean premixed flames, and hydrogen-air mixtures in particular, are subject to a variety of flame-induced hydrodynamic and combustion instabilities that render robust flame stabilization difficult. The present study is concerned with the behavior of lean premixed hydrogen-air flames in a turbulent environment. We focus on flames at atmospheric pressure and in relatively low levels of turbulence characteristic of low-swirl burner experiments [1]. Under these conditions, lean hydrogen-air flames form cellular burning structures due to preferential diffusive thermal instabilities [2,3].

Premixed hydrogen combustion has been the subject of numerous experimental and numerical investigations. Goix et al. [5,4] looked at fractal properties of the flame front. Wu et al. [6,7] studied effects of preferential diffusion. Goix et al. [8] and Kwon et al. [9] studied the turbulent flame brush. Turbulent burning velocity has been measured by Kido et al. [10] and Aung et al. [11]. Cellular structures have been observed in dilute H_2/O_2 mixtures by Bregeon et al. [12] and Mitani and Williams [13]. A related phenomena is the tip opening in lean Bunsen flames observed by Mizomoto et al. [14] and Katta and Roquemore [15]. Lee et al. [17,16] observe strong dependence on curvature in the interaction of lean premixed hydrogen flames with Karman vortex streets. Chen and Bilger [18] present data showing cellular structures in a turbulent Bunsen flame and provide detailed scalar measurements of a progress variable, OH and scalar dissipation rate at lean conditions.

Hydrogen combustion has also been studied using DNS techniques with detailed chemistry in an idealized configuration. Two-dimensional examples include Baum et al. [19], Chen and Im [20], Charntenay and Ern [21], and Im and Chen [22]. More recently Tanahashi et al. [23,24] performed simulations for turbulent premixed hydrogen flames at stoichiometric conditions with detailed hydrogen chemistry in three dimensions.

In this study, we use numerical simulation to obtain a detailed characterization of lean premixed hydrogen flames in three dimensions, allowing us to quantify the interplay between the turbulent fluctuations and hydrogen's natural instabilities, in terms of global flame propagation properties, three-dimensional flame geometry, and detailed chemical structures. In order to minimize analysis complexity, we conduct this study using an idealized computational configuration similar to the studies cited above. A time-dependent three-dimensional flame propagates toward an inflow boundary where turbulent fluctuations have

been superimposed on a mean flow. The fluctuations are chosen to match (in terms of integral scale and intensity) those observed in related laboratory experiments. For this study, the mean inflow velocity is adjusted dynamically using an automatic control algorithm [25] to hold the mean position of the flame a fixed distance above the inflow face. The procedure allows the simulation of a weakly turbulent flame in a quasi-steady configuration without the need to simulate a pilot or some geometric stabilization device. Bell et al. [26] used this control algorithm to explore Lewis number effects in two dimensions.

The goal here is to quantitatively characterize the geometry of the cellular burning front and local burning properties along that front. Capturing this behavior requires that we resolve the interplay of chemistry and transport processes with the turbulent flow, which, in turn, requires detailed models for transport and chemistry. Moreover, the evolution involves a large range of temporal and spatial scales, both in terms of the turbulent spectra and the local flame structure. Here, the simulations are performed using a well-established low Mach number integration methodology that is summarized briefly in the next section. The subsequent section describes the details of the simulation study. Analysis of the simulation results is presented in section 4.

2   Computational Methodology

The simulations presented here are based on a low Mach number formulation [27] of the reacting flow equations. The methodology treats the fluid as a mixture of perfect gases. We use a mixture-averaged model for differential species diffusion (see [28] for complete discussion of this approximation) and ignore Soret, Dufour, gravity and radiative transport processes. With these assumptions, the low Mach number equations for an open domain are

$$\frac{\partial \rho U}{\partial t} + \nabla \cdot \rho U U = -\nabla \pi + \nabla \cdot \tau, \tag{1}$$

$$\frac{\partial \rho Y_m}{\partial t} + \nabla \cdot U \rho Y_m = \nabla \cdot \rho D_m \nabla Y_m - \omega_m, \tag{2}$$

$$\frac{\partial \rho h}{\partial t} + \nabla \cdot U \rho h = \nabla \cdot \lambda \nabla T + \sum_m \nabla \cdot h_m \rho D_m \nabla Y_m \tag{3}$$

where ρ is the density, U is the velocity, Y_m is the mass fraction of species m, h is the mixture enthalpy, T is the temperature, and ω_m is the net destruction rate for species m due to chemical reactions. The perturbational pressure, $\pi(x, t) = p(x, t) - p_0(t)$ where p_0 is the ambient pressure. Low Mach number asymptotic analysis shows that $\pi/p_0 \sim M^2$, where M is the Mach number, $\|U\|/c$, and c is the sound speed. Also, λ is the thermal conductivity, τ is the stress tensor, and $h_m(T)$ and D_m are the enthalpy and species

3

mixture-averaged diffusion coefficients of species m, respectively. The transport coefficients, thermodynamic relationships and hydrogen kinetics (chemical source terms) are obtained from the GRI-Mech 2.11 model [29] with the relevant carbon species removed. This chemical model was selected from a large number of detailed hydrogen mechanisms. Amongst available hydrogen mechanisms under development in the community there is considerable variability in flame properties at the lean conditions considered here. Furthermore, as is well known, at these conditions the flame are thermodiffusively unstable, making measurements very difficult. Consequently, there is no clearly preferred mechanism at these conditions. We selected the hydrogen subset of GRI-Mech 2.11 because it resulted in predictions that are consistently intermediate to the extremes predicted by the leading mechanisms.

The evolution equations (Eqs. (1)–(3)) are supplemented by an equation of state for a perfect gas mixture:

$$
p_0 = \rho R_{mix} T = \rho \mathcal{R} T \sum_m \frac{Y_m}{W_m} \tag{4}
$$

where W_m is the molecular weight of species m, and $\mathcal{R}$ is the universal gas constant. For the present study, we fix p_0 to 1 atm, constant in time and space. Note that this low Mach number system does not admit the propagation of acoustic waves, which cannot be supported physically in a domain of the size investigated here [27].

The basic discretization [30] combines a symmetric operator-split treatment of chemistry and transport with a high-resolution fractional step approach for advection. A density-weighted approximate projection [32,31] ensures that the evolution (Eqs. (1)–(3)) satisfies the constraint imposed by the equation of state, Eq. (4) [33]. Elimination of the (negligible) acoustic wave propagation from this system enables numerical evolution at the time-scales of advective transport, and a resulting order-of-magnitude gain in overall integration efficiency. Diffusion and chemical kinetics, which occur on time scales faster than advection, are treated time-implicitly. An automatic feedback control algorithm [25,34] adjusts the inflow velocity to stabilize the flame in the computational domain. This integration scheme is embedded in a parallel adaptive mesh refinement framework based on a hierarchical system of rectangular grid patches [35]. The overall adaptive integration algorithm is second-order accurate in space and time, and discretely conserves species mass and enthalpy. Implementation of the adaptive projection scheme makes efficient use of distributed-memory parallel computing architectures; a dynamic load balancing algorithm [36] accomodates the heterogeneous and time-dependent workload associated with chemical kinetics near the evolving flame surface, as localized patches of grid refinement are created and destroyed during the simulation. The reader is referred to [30] for details of the low Mach number

model and its adaptive implementation.

The adaptive low Mach number integration algorithm has been used for a broad array of laminar and turbulent time-dependent premixed flame studies. Example laminar fluid-flame interaction studies include experimental validation and analyses of the interaction of single vortical structures with a rich methane-air flame [37]. In [25,38], the control algorithm discussed above was presented and used to explore the response of methane-air flames in the presence of turbulence, based on the detailed chemistry and transport models in the GRI-Mech 3.0 mechanism [39]. A two-dimensional controlled hydrogen flame in the turbulence/chemistry regime of the present work was analyzed extensively in [26]. This low Mach number methodology was also used to understand and characterize turbulence/flame interactions in three-dimensional premixed flames at the full scale of laboratory experiments. Studies of this type include a rod-stabilized premixed turbulent V-flame experiment [40], and a piloted slot Bunsen burner [41]. For the laboratory-scale studies, the computed flame shapes and locations, as well as the velocity fields, were characterized statistically and validated with measured experimental data.

3 Case Study

The idealized flow configuration we consider, schematically identical to that used by Tanahashi and coworkers (see [23], Fig. 1), initializes a slightly perturbed, flat, laminar flame in a rectangular domain oriented so that the flame propagates downward (since gravity is not included, the direction is for orientation only). A cold ($T = 298$ K) turbulent H_2-air premixture ($\phi = 0.37$) enters the domain through the square bottom boundary, which measures 3 cm on a side. Hot combustion products exit the domain through the top, 9 cm downstream. Lateral computational boundaries are periodic. The inlet boundary conditions are Dirichlet for all state quantities, and are applied directly at the cell face on the domain boundary. Along the outflow boundary, Neumann (zero-gradient) conditions apply. The pressure, π, satisfies Neumann conditions at the inlet, and homogeneous Dirichlet condition on the outflow face. For the specified inlet conditions using the hydrogen subset of GRI-Mech 2.11 used for the three-dimensional studies, the PREMIX code [42] predicts a laminar burning speed, $s_L = 15.2$ cm/s and a thermal flame thickness, $\delta_L = (T_b - T_u)/\|\nabla T\|_{max} = 0.8$ mm, where $T_b - T_u$ is the temperature jump across the (idealized) flat flame, and $\|\nabla T\|_{max}$ is the peak temperature gradient within the flame structure.

Turbulent fluctuations are generated in an auxiliary DNS calculations performed using IAMR [43], an incompressible viscous flow solver, in a triply-periodic cubic domain measuring 3 cm on a side. Initial conditions corre-

5

sponding to an array of 3 mm jets, adjusted to have zero mean and perturbed to break symmetry, are evolved until the flow is fully turbulent and a desired turbulent intensity is reached. This approach generates zero-mean turbulent fluctuations with integral scale $\ell_t = 3$ mm $= 3.75 \cdot \delta_L$ in the mean flow direction, and anisotropies characteristic of plate turbulence. These fluctuations are added to the mean velocity at the domain inlet to introduce turbulence into the fuel stream.

Since the hydrogen-air flame at $\phi = 0.37$ is thermodiffusively unstable we first consider the case with a uniform inflow stream (no turbulent fluctuations) in order to capture the evolution of the flame surface under the influence of the natural instability. In addition, we consider two turbulent cases, with intensities of 11 cm/s and 43 cm/s ($u'/s_L = 0.72$ and 2.8), which we will refer to as the "weak" and "strong" cases, respectively. These values span a range of measured conditions at this integral length scale for typical lean premixed hydrogen flames stabilized in a low-swirl burner [44] experiment. The Kolmogorov length scales for the turbulent cases are approximately $\eta = 345$ μm and 122 μm for the weak and strong conditions, respectively.

A uniform base grid of 128$\times$128$\times$384 cells is used in all cases. Adaptive mesh refinement is used to dynamically place additional factor-of-two grid resolution in a subregion of the domain extending from the inlet face and through the combustion reaction zone, which is wrinkled over time by the turbulence and the flame's thermodiffusive properties. The strategy for dynamic adaptive grid placement leads to a mesh spacing upstream of the flame with $\Delta x = 117 \mu$m, which is sufficient to accurately resolve the turbulent flow from the inlet face through to the flame surface. (See Aspden et al. [45] for a detailed discussion of the performance of this algorithm for evolving non-reacting turbulent flows). Due to volumetric expansion across the flame, a significant increase in fluid viscosity of the products, and the lack of significant fine-scale chemical processes downstream of the flame, the base grid is sufficient to resolve the flow beyond combustion zone. This level of resolution is used to evolve the system until a statistically stationary flame is established using feedback-controlled inlet flow. Prior to gathering detailed statistics discussed below, an additional factor of two refinement was added to the calculations. The extra refinement level was triggered dynamically by the presence of the flame radical, atomic hydrogen, and resulted in an effective resolution of 58.6 μm at the flame surface. In this final configuration, the finest level grids occupied 6-12% of the computational domain, depending on the intensity of the inflowing turbulence; the intermediate refinement levels occupied 34-44% of the domain. Using this final refinement strategy, the simulation was evolved over a time interval $\Delta t \approx .35\tau_\ell$, where the integral eddy turnover time, $\tau_\ell = \ell_t/u' = .027, .007$ s for the weak and strong cases, respectively, to provide statistics of the flame propagation. A comparable number of steps were taken at the final resolution for the no-turbulence case. Statistics gathered included the local burning rate,

flame thickness, and curvatures. Analysis of the errors indicate that at this resolution the turbulent flame speed is accurate to approximately 0.6%.

4 Results

In the following, we characterize the time-dependent evolution of the three quasi-stationary lean hydrogen-air flames in three ways. First, we provide a qualitative description of the salient features of the flames, and discuss global propagation characteristics and how they are affected by the level of inlet turbulence. We then discuss the flame geometry including a topological analysis of the cellular flame surface to capture the distribution of cell-sizes associated with these flames. Finally, we present a number of diagnostics to quantitatively relate the behavior of these flames to the one-dimensional flat-flame idealization computed using the PREMIX code.

4.1 Global flame properties

Fig. 1(a) shows the time history of the mean inlet velocity for the three flames, which is equivalent to the turbulent flame speed once the flame location has stabilized. The figure also includes a typical plot of the mean flame location taken from the no-turbulence case, and demonstrates that the flame location stabilizes very quickly. Over the duration of the simulations, the flame position remains locked to within a couple of microns of the control location.

[Fig. 1 about here.]

As expected from the experimental literaure (see, for example, [12,13]), the initial weakly-perturbed flat flame quickly rolls into cellular burning structures that are separated by regions of local extinction, even in the no-turblence case. This type of burning structure has also been observed in 2D lean hydrogen simulations at even higher turbulence intensities (e.g. [20,22]) with constant Lewis number transport models. These cellular burning structures tend to drift and change shape in the frame of the calculation on a time-scale that roughly corresponds to the motion of the largest eddies in the turbulent inflow. The burning cells are clustered near the $T = 1200$ K isotherm, which undergoes slow large-scale cusping and distortion. Extinction regions develop in the flow continuously, either smoothly extending pre-existing regions, or through spontaneous splitting of large burning cell structures. Fig. 1(b) is a snapshot of the T=1200 K isotherm, taken at $t = \tau_\ell$ for the strong case, and is qualitatively typical of all three flames over most of the computed evolution. The burning in the cells is extremely intense, with peak fuel consumption rates more than

7

three times that of the flat laminar flame at this equivalence ratio. The combination of increased flame area and localized consumption rate intensification leads to a dramatic increase in global burning rate. Associating the mean (controlled) inlet velocity with the instantaneous turbulent burning speed of these flames, we observe values of approximately $4s_L$ for the case with no turbulence, $5s_L$ for the weak turbulence case and $8s_L$ for the strong turbulence case. (We note however, that the instantaneous turbulent flame speeds show considerable variability, as shown in Fig. 1(a). In fact, it is not clear whether or not the instantaneous flame speeds are statistically stationary, particularly for the strong turbulence case.)

[Fig. 2 about here.]

The observed intensification of the burning results from differential diffusion. Differential diffusion near the flame surface leads to a strong local modulation of mixture composition in both flat and curved flames. However, enhanced transport effects in the multi-dimensional case leads to a flame that is effectively enriched in some places, relative to the flat flame solution ([2,3]). Following the analysis of [18] for stretched laminar flames, we quantify this effect in Fig. 2, which shows JPDFs of the variation of the local atomic stoichiometry, $\phi^\ell = 0.5\,[\mathrm{H}]\,/\,[\mathrm{O}]$, for each of the three cases computed. In the definition of ϕ^ℓ, the concentration, $[x]$, represents the total number of atoms of type x in the molecules making up the mixture. Coloring of the JPDF in Fig. 2 indicates the log of the joint probability distribution; the overlayed curves correspond to ϕ^ℓ as a function of T in the flat flame solutions over a range of inlet mixtures. As the flame is approached, H_2 and O_2 are consumed chemically, driving a diffusive flow of both molecules downstream toward the flame. The larger diffusivity of hydrogen gives rise to a higher diffusion velocity, and corresponding drop in H concentration, relative to O. Downstream of the flame, in the absence of significant chemical sources, the mixture ratio returns to its inlet value. Fig. 2 shows a relatively broad distribution of ϕ^ℓ as a function of temperature for all three cases. However, all the cases show that the most probable distribution follows the ϕ^ℓ curves corresponding to a global equivalence ratio of $\phi \approx 0.43 - 0.45$. We also note that in the $T = 900 - 1200$ range the ϕ^ℓ is continuing to increase relative to the laminar curves, indicating that the flames are continuing to be enriched. Note also that enrichment is somewhat enhanced for the stronger turbulence case. This enrichment leads to post-flame temperatures that are higher than the $\phi = 0.37$ adiabatic flame temperture, with values corresponding to flat laminar flames in the $\phi \approx 0.45 - 0.47$ range. The figure also shows a broad distribution of temperatures in the $T = 1000 - 1500$ range at the lower end of the range of local ϕ^ℓ's at those temperatures. The lower temperatures in that range correspond to the fluid passing through the non-burning regions that are heated by thermal conduction while the higher ranges represent the terminal conditions of the intense burning. This variation in temperature slowly equilibrates down-

8

stream of the flame as thermal conduction and turbulent mixing homogenize the product mixture.

4.2 Flame Surface Definition

[Fig. 3 about here.]

In the following sections, we will examine the local structure of the flame in more detail. As part of this analysis, we will examine the flame geometry and quantify the combustion rate variability along the flame. To do this, we must define a *reaction progress variable*, which should be monotonically increasing through the flame, from reactants to products and identify the "flame" with a specific isovalue of the progress variable. In steady one-dimensional flat flames, good candidates are fuel concentration and the temperature field; the choice is usually dictated by the type of experimental or theoretical diagnostic required for the analysis. For the thermodiffusively unstable flames considered here, defining such a quantity is problematic, as illustrated in Fig. 3(a). The figure shows the behavior of the temperature and fuel contours relative to the local consumption rate. We have drawn a single contour of the temperature and fuel concentration for clarity; the value selected for each is taken from the location of peak fuel consumption, $\omega_{H2} = \omega_{max}$, in the PREMIX-computed flat flame solution for inlet mixture of ϕ=0.37. The consumption rate in the plot is normalized by ω_{max}, and the minimum colored value, $\omega_{H2} = \omega_{min} = 1 \ kg_{H2}/m^3s$, corresponds to the 98$^{\text{th}}$ percentile of fuel consumption—that is, 98% of the H$_2$ consumed in the domain occurs in the colored regions where $\omega_{H2} \geq \omega_{min}$.

Fig. 3 shows a typical slice through one of the simulations showing gaps in the flame surface. Contours of temperature and fuel concentration both define a path across the gap but these are unrelated to the "flame" because there is essentially no burning. Moreover, we observe a significant decoupling of the fuel and temperature contours, particularly in regions where the fuel consumption rate is significantly lower than the peak values. Fig. 3(b) shows a close-up of the fuel and temperature contours, and their geometry relative to the burning cells in a region near the slice taken in Fig. 3(a). In this second plot, the contour of fuel consumption, $\omega_{H2} = \omega_{max}$, forms closed green surfaces and roughly indicates the three-dimensional boundary between burning cells.

[Fig. 4 about here.]

As a quantitative measure of the relative alignment of two candidate reaction progress variables (temperature and fuel concentration), we compute the angle, θ, between their normals. The distribution of this angle along the flame surface can be computed over the entire volume. However, we are interested

in this measure only in regions of nontrivial consumption. Fig. 4 shows the "moment" of the distribution of $\cos\theta$ vs. consumption rate, where the moment is with respect to the local value of consumption (ie, the PDF of $\cos\theta$ vs. ω_{H2} is scaled locally by ω_{H2}). The resulting distribution then integrates to the total reaction rate over the domain, and reflects the conditions where nontrivial consumption occurs. The result is typical of all three cases and is invariant over time. The data shows that where there is non-trivial fuel consumption, the fuel and temperature normals are essentially anti-parallel (ie, $\cos\theta = -1$). Conversely, in regions of vanishing consumption, the vectors become somewhat decorrelated. Similar observations were made qualitatively in [18], in the context of lamella-like flame structures. Thus, provided that subsequent analysis is confined to burning regions, the two scalars will provide comparable measures of reaction progress.

This suggests that to perform a more detailed analysis of the local flame structure, we need to exclude the portion of the contour of the progress variable that passes through the gaps. Thus, we will define the flame as the portion of the contour over which the fuel consumption rate is above a given threshold. While our definition makes intuitive sense, and appears to be robust near the region of nontrivial fuel consumption, it does imply an arbitrary division of the computed solution (even in cold regions) into "flame" and "no-flame" regions. However, because the contours can make large excursions that are unrelated to the combustion process as they cross the gap, failure to exclude that portion of the contour from the definition of the "flame" can lead to anomalous statistical behavior.

For the analyses present here, we will use a characterization of the flame based on temperature. In particular we identify the flame with the $T=T_{\omega-max}$ isotherm where $T_{\omega-max}$ is the value of temperature at the point of peak fuel consumption in the flat laminar flame. We extract the "flame" as a triangulated surface representing this isotherm using the standard marching cubes algorithm and linear interpolation of the solution field over a hierarchical system of rectangular grid patches. A well-known feature of the marching cubes surface extraction procedure is the generation of many poorly shaped triangles (long, narrow triangles with relatively small areas). The QSlim [46] algorithm is used to decimate this original triangulation to remove such cases, and provide a reduced representation that more uniformly tiles the flame surface. We then exclude non-burning regions (unless otherwise noted) by conditioning on $\omega_{H2} > 0.35 \times \omega_{H2}^{max}$, where ω_{H2}^{max} is the maximum of the fuel consumption rate in the flat laminar flame at $\phi = 0.37$. We note that because of the enhanced burning, this value is approximately 5% of the peak value of fuel consumption in the three-dimensional flames. Although this cutoff value is arbitrary and can have slight effects on the results, the overall trends remain unchanged and, as noted above, including the full contour introduces significant artifacts because of the essentially arbritrary way the isocontour bridges the gaps in

the flame.

4.3 Flame Geometry

With the definition that the "flame" is an isotherm, conditioned on fuel consumption rate, we first examine the geometry of the flame by computing the curvatures of this surface. The two principal curvatures, κ_1 and κ_2, of the flame are implicit functions of the temperature field over all space in each snapshot of the computed solutions. We define as positive curvature the case where the center of curvature is in the products region. The mean curvature, $K = \kappa_1 + \kappa_2$, may be evaluated in all space near the flame surface, and in particular, is interpolated to the $T=T_{\omega-max}$ isotherm. In practice, rather than explicitly computing κ_1 and κ_2, K may be computed more simply using the identity, $K = -\nabla \cdot \vec{n}$, where $\vec{n}$ is a unit vector locally aligned with the temperature gradient. This field is then interpolated to the $T=T_{\omega-max}$ isotherm, and in Fig. 5(a) we plot the area-weighted PDF of the local mean curvature, K (scaled by the thermal thickness, δ_T of a laminar flame at $\phi=0.37$) of the burning regions for all three flames averaged over all timesteps of the quasistationary data at the finest resolution. Properties of the distribution are given in Table 1. The data shows a positive peak in the mean curvature distribution for all three flames, indicating that the burning cells are predominantly convex with respect to fuel. We note that the most probable mean curvature is quite small (0.267 - 0.340) relative to the thermal thickness of the flame indicating that the most probable radius of curvature is 3-4 flame thicknesses. The standard deviation, skewness and kurtosis of these distributions show no clear trend with increasing turbulence levels, but we do observe a 20% decrease in the mean value with both turbulence levels compared to the no-turbulence case. This reduction is due to a significant decrease in larger positive curvatures (a sudden drop for any turbulence level), and a gradual increase in flat or negatively curved regions with increasing fluctuation intensity. These observations of mean curvature in 3D can be contrasted to results reported in [18] for 2D curvatures. They report near zero mean values and a negative skewness, whereas our 3D measurements show a positive mean and skewness. Consistent with our observations, they observe no clear trend with turbulence fluctuation intensity.

[Fig. 5 about here.]

[Table 1 about here.]

[Table 2 about here.]

The Gaussian curvature, $G = \kappa_1\kappa_2$, may also be computed easily given the unit normal, $\vec{n}$, over all space. Fig. 5(b) shows the flame surface area-weighted

11

PDF of the Gaussian curvature (scaled by δ_T^2). Properties of this distribution are given in Table 2. The positive peak in the Gaussian curvature indicates that the burning occurs in "spherical" regions as opposed to "saddle" ($G < 0$) or "cylindrical" ($G = 0$) configurations. Significantly, this is opposite to the trend observed in lean methane flames (with unity Lewis number) in which the Gaussian curvature is skewed toward saddles (cf. [41]). In all three cases, the distributions have a high positive skewness indicating a further bias to spherical structures. The mean value of the Gaussian curvature decreases by over 40% for both the low and high turbulence cases compared to the no-turbulence case, demonstrating that even low-level turbulence tends to dramatically reduce the prevalence of larger spherical features on the flame surface, while the occurence of flat and saddle-shaped regions increase somewhat more uniformly with fluctuation intensity.

The other key characteristic of the flame geometry is the cellular structure. Fig. 1 shows that the flame surface consists of intensely burning patches separated by local extinction regions. To obtain a more quantitative description of the cellular structure, we investigate the distribution of the sizes of the burning patches. To compute this distribution, we perform a topological analysis using a set of tools based on Morse theory [48,47]. Specifically, the goal of this analysis is to determine the number of burning patches over time, and how the areas of those patches are distributed. We use an approach that enables a complete segmentation of the gradient flow of a scalar field in a surface without relying on derivative estimates or numerically driven computations, avoiding numerical instabilities as well as error propagation. This approach has been applied successfully in other contexts to the analysis of the mixing layer of simulations of Raleigh-Taylor instabilities [49] and to the dynamic analysis of the complex structure of porous media under stress and failure [50].

The flame was divided into individual burning cells by computing a hierarchical Morse complex segmentation of the flame isotherm, based on the gradient flow [51] of H_2 consumption, ω_{H2}. In particular, each local maximum of fuel consumption corresponds to a region that is defined as the set of points whose gradients converge towards this maximum. The hierarchical model allows merging pairs of adjacent regions based on persistence, which is the difference in function value between the saddle separating the two regions and the lower of their maxima. In this way one can reliably segment regions that persist only at high variations of function value.

We have again used $\omega_{H2} > 0.35 \times \omega_{H2}^{max}$ as the threshold to define the boundary of the burning patches. For this analysis, we found that a slightly warmer isotherm at T=1225 K gives more stable results. This is because the locally richer flame regions show a peak in fuel consumption at higher temperatures, consistent with the behavior of richer flat flame solutions. With these choices of parameters, the analysis gave extremely stable measurements over a broad

range of persistence values.

Over each of the three simulations, the evolution produced roughly 100 data files at the finest (3-level) AMR resolution, separated in time by 24 μs. The Morse-Smale segmentation determines the number and sizes of the burning cells at each time step . The average number of burning cells at any given time is approximately 30-31 for the no- and strong-turbulence cases, but decreases to approximately 24 for the weak-turbulence case. Thus there is no particular trend in the number of patches with turbulence intensity. And while the data showed that the number of patches was statistically stationary over the time window considered with a moderate level of fuctuations in time, a more detailed analysis shows that over this period, there are a significant number of "birth" and "death" events for individual cells. In Fig. 6, we present an area-weighted cumulative distribution of patch areas, formed as a running accumulation of the cell areas, sorted in ascending order, and normalized to the final sum. Here, the CDF at a given ordinate is then the total fraction of flame area contained in cells with individual areas less than the absissa. The results of the analysis are somewhat counterintuitive. The CDF's, which are approximately linear, are increasingly broad with increasing levels of turbulence, indicating a shift toward patches with larger areas with increasing turbulence. In particular, the data shows that with no turbulence, 19% of the area is contained in patches larger than 1 cm^2. This increases to 65% for the weak turbulence case and 81% for the strong turbulence case. We note that the area-weighted CDF emphasizes large patches. Examining the distribution of smaller patches shows that approximately 40% of the patches have areas less than 0.3 cm^2, independent of the turbulence level. The data can also be used to compute the flame surface area conditioned on burning. The average available burning areas, normalized by the cross-sectional area of the simulation domain are 1.4, 1.8, and 2.8 for the none, weak and strong turbulence levels, respectively.

4.4   Local Flame Structure

In order to analyze the local flame structure in more detail, we first construct a local coordinate system based on the thermal field near the flame. Beginning with the flame surface as defined in the section above, we use a fourth-order Runge-Kutta scheme to construct the integral curves of the temperature gradient field in both directions away form the surface. The resulting paths extend from cold regions upstream of the flame, through the surface, and downstream into the products region. Data is then sampled along these paths to provide a representation of the solution in the local flame coordinate system. Addi-

13

tionally, the connectivity of the flame surface is used to construct localized prism-shaped volumes, Ω, based on these integral curves, as depicted in Fig. 7. The construction is analogous to the two-dimensional procedure discussed in [52,25]. These volumes have a triangular intersection, τ (area $= A$), with the flame surface. The end caps of the volumes lay entirely in the hot or cold regions far from the flame surface. Discrete volumes constructed in this way are disjoint, and their union is the entire consumption layer above the threshold at this snapshot in time.

[Fig. 7 about here.]

4.4.1 Consumption-based flame speed, s_c^ℓ

We define a local consumption-based flame speed on Ω by analogy to the one-dimensional flame solutions. In effect, we associate the local volumetric consumption of fuel with the propagation of a "flame" defined on the triangle τ. More precisely, we obtain an expression for the consumption-based flame speed, s_c^ℓ, by dividing the volume-integral of the consumption rate by the area A. Normalizing by the inflowing fuel density $(\rho Y_{H_2})_{in}$, we obtain

$$s_c^\ell = \frac{1}{A\,(\rho Y_{H_2})_{in}} \int_\Omega \omega_{H_2} d\Omega \tag{5}$$

Typically, this quantity will be normalized by the flat flame burning speed, s_L, obtained from the corresponding PREMIX flame solution at $\phi = 0.37$. Eq. 5 has the property that the global burning speed is the area-weighted average of s_c^ℓ, provided the set of wedge volumes in the sum includes all regions of significant fuel consumption. Note also that the QSlim processing removes small triangles from the flame, and is necessary to avoid poorly conditioned evaluation of Eq. 5, due to the appearance of A in the denominator.

4.4.2 Flame Curvature vs. s_c^ℓ

Fig. 8 shows the consumption-rate moment of the JPDF of the mean curvature versus the local consumption speed, s_c^ℓ, for the three cases. Similar to the data shown in Fig. 4, the consumption rate moment is used to weight the PDF so that its integral becomes the total consumption rate over the domain. This diagnostic depicts the dependence of local burning speed on curvature, with a bias towards more vigorously burning regions. The positive slope of these correlations can be interpreted as a negative effective turbulent "Markstein" number, and is characteristic of the thermodiffusive instability—bulges of the flame surface into the fuel tend to accelerate the local burning rate, and bulges into the products tend to extinguish locally. Although there is considerable

14

spread in the data, the dependence of the local consumption speed on curvature appears to depend on turbulence intensity, with the correlations being less sensitive with increasing turbulence. This suggests that turbulent mixing is serving to moderate the thermodiffusive instability somewhat. The figures also show that the most probable local burning speed is approxmiately 2.5 s_L for the no-turbulence and weak-turbulence case, and increases to 3.0 s_L for the strong-turbulence case. Significantly, the most probable local burning speed at zero curvature is considerably higher than the

[Fig. 8 about here.]

laminar flame speed. We also note that for the no-turbulence case, the most probable local burning speeds span a broader range of values than in the turbulence cases. The most probable burning speed in the strong turbulence case also occurs at a higher mean curvature, indicating that the turbulence is able to wrinkle the flame on smaller scales than the "natural" wrinkling associated with the thermodiffusive instability.

The trends we observe with increasing turbulence levels suggest that fluctuations, at even the lowest intensity levels, appear to suppress to some extent the growth and propagation of the spherical burning cells characteristic of the thermo-diffusive instability, even though the effects of the instability are clearly present in all the runs. The distribution of local burning speeds and the flame area characterization in Fig. 6 show that although there is some local intensification with increasing turbulence, the changes in flame surface area play a dominant role in increase the global turbulent burning speed.

[Fig. 9 about here.]

4.4.3   Local Flame Intensification

In this section, we explore two different metrics for quantifying the local flame intensification discussed above. First, we consider the correlation of local burning speed and peak temperature gradient, which characterizes the chemical heat release. Along each of the integral curves used in the construction of the local burning speed we extract the peak temperature gradient. In Fig. 9, we plot the JPDF of peak thermal gradient normal to the flame and local consumption-based flame speed for the case of strongest turbulence (the corresponding plots for the other cases are virtually identical, save for a small shift in the peak consumption speed that was discussed above). For reference, the JPDF is overlayed with the corresponding variation of the flat flame solution. The JPDF shows a broad variation in the local burning conditions; however the most probable conditions show heat release rates ($max(||\nabla T||)$) and local consumption speeds characteristic of $\phi = 0.43 - 0.47$ flames, consistent with more global observations discussed above.

15

As a second diagnostic, we investigate the correlation of temperature and fuel mass fraction in a neighborhood of the flame. In particular, we compute the JPDF of T and $X(H_2)$ over the region covered by the local coordinate system defined over the unconditioned flame surface, which is shown in Fig. 10(a).

[Fig. 10 about here.]

The component of this JPDF corresponding to intensely burning regions can be isolated by considering only the flame volumes for which $X(H_2) > 0.0104$ on the $T = 1139$ isotherm. This threshold $X(H_2) = 0.0104$ corresponds to the intersection of $X(H_2)$ surface and isotherm in Figure 3 and corresponds, roughly, to flames burning with the intensity of a $\phi = 0.37$ flame. The intensely burning component and its complement are shown in Figures 10(b) and 10(c), respectively. Figures 10(a) and 10(b) are fairly similar, indicating that the intense burning represents the dominant behavior of the flame. The overlay of the laminar flame solutions on Figure 10(b) show that the fuel and temperature correlation is consistent with an enriched flame with $\phi = 0.43 - 0.47$, again consistent with other measures of the intensification discussed above. The non-intensely burning JPDF shown in Figure 10(c), shows no strongly dominant distribution. Part of the distribution suggests weakly burning flames at reduced equilvalence ratios, with much of the distribution lying below the $\phi = 0.31$ flame curve where there is essentially no H_2 fuel consumption. The most pronounced feature in Figure 10(c) is a band of temperatures at low fuel concentration, which corresponds to the slow diffusive heating of the fluid in the non-burning region of the flame surface.

4.4.4 Species Transport

To understand the mechanism that leads to local intensification, we need to look at diffusive species transport in more detail. Since the contours of temperature and fuel concentration are not aligned, there is a component of fuel transport along the flame front. The diffusive flow of fuel normal to the temperature gradient (ie, in the flame surface) is:

$$\vec{\Gamma}_{H2}^{T} = (I - \frac{qq^{T}}{||q||^2})\vec{\Gamma}_{H2} \tag{6}$$

where $\vec{\Gamma}_{H2} = -\rho D_{H2}\nabla Y_{H2}$ is the diffusion flux of H_2, D_{H2} is the mixture-averaged diffusivity of H_2 molecules, and $\vec{q} = -\lambda \nabla T$ is the heat flux. Fig. 11(a) shows a typical flame isotherm from the strong turbulence case, colored

[Fig. 11 about here.]

16

locally by the fraction of the diffusive flux that is aligned locally with the flame surface, $\|\vec{\Gamma}_{H2}^{T}\|/\|\vec{\Gamma}_{H2}\|$ (the surface shown is conditioned on $\omega_{H_2} < 0.35\omega_{max}$ in order to eliminate the downstream excursions of the isotherm and simplify the graphic). The view angle is from within the fuel stream looking upward at the underside of the flame surface. There is a strong parallel diffusive tranpsort of fuel near the edges of the cellular burning structures that decreases quickly to zero in the central part of the cells. Fig. 11(b) shows the divergence of this fuel mass flux in the surface, and indicates that fuel is transported out of the cusped zones, and into the edges of neighboring cells. Fig. 11(c) shows the distribution of transport in the isotherm, $T = T_{\omega-max}$, for both H_2 and O_2 over the entire surface at this snapshot in time. Over most of the burning region, there is a nontrivial transport of H_2 in the flame surface that is not mirrored by flow of O_2; almost all of the diffusive transport of O_2 is normal to the flame surface. The resulting differential transport between fuel and oxidizer leads to variations in the local stoichiometry that results in the observed enrichment of the fuel, which in turn, leads to the intensification of burning in the cells.

5   Conclusions

We have numerically stabilized lean premixed hydrogen flames in a turbulent fuel stream using a feedback control algorithm. Depending on the turbulence level, we observe flames that propagate globally at 3-8 times the speed predicted by a one-dimensional idealization of these thermodiffusively unstable flames. The quasi-steady flames burn intensely in time-dependent cellular structures that are separated by fuel-depleted regions that do not burn. The cellular structures tend to be convex with respect to the fuel and have positive Gaussian curvature. The cellular burning patterns were divided into individual cells by computing a segmentation of the flame isotherm based on a threshold level of local fuel consumption. This analysis shows that approximately 40% of the patches have areas less than 0.3 cm^2, independent of the turbulence level. The analysis also shows a increase in flame area with increasing turbulent intensity. Somewhat surprisingly, we also saw a clear increase in the size of the largest cells with increasing turbulence.

Classical flame theory suggests that positively-curved regions are enriched with highly-mobile (fuel) molecules, leading to a positive correlation of local flame speed with curvature. Analysis of the local flame speeds confirms this correlation. It also shows that overall effect of this correlation weakens with increasing turbulence suggesting that turbulent mixing is modulating the effective Lewis number. We also observe that the mean propagation speed in locally flat regions of these flames is significantly higher than the corresponding idealized one-dimensional laminar flame. This increase in local burning speed is a result of a local enrichment of the fuel due to differential diffusion.

For the $\phi = 0.37$ mixture considered here, the local burning characteristics are comparable to adiabatic 1D flames at $\phi \approx 0.43 - 0.47$.

The high global turbulent flame speed of these flames results from both an increase in flame surface area and the local enhancement of the burning. Approximation of turbulent flame speed by the flame surface area multiplied by the laminar flame speed significantly underpredicts the overall burning. However, once the local intensification is taken into account, although the intensification increases with turbulent intensity, the dominant effect on increasing turbulent flame speed is the increase in available flame surface area.

Recent work by Grcar *et al.* [53] has shown that freely propagating lean hydrogen flames in this regime are effected significantly by the the Soret effect. In laminar 2D cases, the Soret effect increases the local burning speeds observed in these thermo-diffusively unstable configurations by almost 20%, and increases the peak thermal gradients. Whether this effect remains important in a turbulent flames is unknown. However, computing approaches to incorporate these effects are presently unsuitable for 3D turbulent simulations. In future work, we plan to develop the numerical capability to incorporate the Soret effects, and apply the analysis methodology developed here to simulations of laboratory experiments that stabilize lean premixed hydrogen flames using a low swirl burner.

Acknowledgments

References

[1] B. Bedat, R. K. Cheng, *Combust. flame* 100 (1995) 485–494.

[2] G. H. Markstein, *The Journal of Chemical Physics* 17 (4) (1949) 428–429.

[3] Y. B. Zeldovich, *Theory of Combustion and Detonation in Gases (in Russian)*, Acad. Sci. USSR, 1944.

[4] P. J. Goix, I. G. Shepherd, *Combustion Science and Technology* 91 (1993) 191–206.

[5] P. J. Goix, I. G. Shepherd, M. Trinite', *Combustion Science and Technology* 63 (1989) 275–286.

[6] M.-S. Wu, S. Kwon, J. F. Driscoll, G. M. Faeth, *Combustion Science and Technology* 73 (1990) 327–350.

[7] M.-S. Wu, S. Kwon, J. F. Driscoll, G. M. Faeth, *Combustion Science and Technology* 78 (1991) 69–96.

[8] P. J. Goix, P. Paranthoen, M. Trinite', *Combustion and Flame* 81 (1990) 229–241.

[9] S. Kwon, M.-S. Wu, J. F. Driscoll, G. M. Faeth, *Combustion and Flame* 88 (1992) 221–238.

[10] H. Kido, K. Nakashima, M. Nakahara, J. Hashimoto, *JSAE Rev.* 22 (2001) 131–138.

[11] K. T. Aung, M. I. Hassan, S. Kwon, L.-K. Tseng, O.-C. Kwon, G. M. Faeth, *Comubstion Science and Technology* 174 (2002) 61–99.

[12] B. Bregeon, A. S. Gordon, F. A. Williams, *Combustion and Flame* 33 (1978) 33–45.

[13] T. Mitani, F. A. Williams, *Combustion and Flame* 39 (1980) 169–190.

[14] M. Mizomoto, Y. Asaka, S. Ikai, C. K. Law, *Proc. Combustion Institute* 20 (1984) 1933–1939.

[15] V. R. Katta, W. M. Roquemore, *Combustion and Flame* 102 (1995) 21–40.

[16] J. G. Lee, T.-W. Lee, D. A. Nye, D. A. Santavicca, *Combustion and Flame* 100 (1995) 161–168.

[17] T.-W. Lee, J. G. Lee, D. A. Nye, D. A. Santavicca, *Combustion and Flame* 94 (1993) 146–160.

[18] Y.-C. Chen, R. W. Bilger, *Combustion and Flame* 138 (2004) 155–174.

[19] M. Baum, T. J. Poinsot, D. C. Haworth, N. Darabiha, *J. Fluid Mech.* 281 (1994) 1–32.

[20] J. H. Chen, H. Im, *Proc. Combust. Inst.* 27 (1998) 819–826.

[21] J. de Charentenay, A. Ern, *Combustion Theory and Modeling* 6 (2002) 439–462.

[22] H. G. Im, J. H. Chen, *Combust. Flame* 131 (2002) 246–258.

[23] M. Tanahashi, M. Fujimura, T. Miyauchi, *Proc. Combust. Inst.* 28 (2000) 529–535.

[24] M. Tanahashi, Y. Nada, Y. Ito, T. Miyauchi, *Proc. Combust. Inst.* 29 (2002) 2041–2049.

[25] J. B. Bell, M. S. Day, J. F. Grcar, M. J. Lijewski, *Comm. App. Math. Comput. Sci.* 1 (1) (2005) 29–52.

[26] J. B. Bell, R. K. Cheng, M. S. Day, I. G. Shepherd, *Proc. Combust. Inst.* 31 (2007) 1309–1317.

[27] R. G. Rehm, H. R. Baum, *N. B. S. J. Res.* 83 (1978) 297–308.

[28] A. Ern, V. Giovangigli, *Multicomponent Transport Algorithms*, Vol. m24 of *Lecture Notes in Physics*, Springer-Verlag, Berlin, 1994.

[29] C. T. Bowman et al., *GRI-Mech 2.11*, available at `http://www.me.berkeley.edu/gri_mech`.

[30] M. S. Day, J. B. Bell, *Combust. Theory Modelling* 4 (2000) 535–556.

[31] A. S. Almgren, J. B. Bell, W. Y. Crutchfield, *SIAM J. Sci. Comput.* 22 (4) (2000) 1139–59.

[32] A. S. Almgren, J. B. Bell, W. G. Szymczak, *SIAM J. Sci. Comput.* 17 (2) (1996) 358–369.

[33] R. B. Pember, J. B. Bell, P. Colella, W. Y. Crutchfield, M. W. Welcome, *J. Comp. Phys.* 120 (1995) 278–304.

[34] J. B. Bell, M. S. Day, A. S. Almgren, M. J. Lijewski, C. A. Rendleman, R. K. Cheng, I. G. Shepherd, *Simulation of Lean Premixed Turbulent Combustion*, Vol. 46 of *Journal of Physics Conference Series: SciDAC 2006 (W. Tang, Ed.)*, Institute of Physics Publishing, Denver, CO, 2006.

[35] M. J. Berger, P. Colella, *J. Comput. Phys.* 82 (1) (1989) 64–84.

[36] C. A. Rendleman, V. E. Beckner, M. Lijewski, in: *Computational Science – 2001*, 2001, pp. 1117–1126.

[37] J. B. Bell, N. J. Brown, M. S. Day, M. Frenklach, J. F. Grcar, S. R. Tonse, *Proc. Combust. Inst.* 28 (2000) 1933–1939.

[38] J. B. Bell, M. S. Day, J. F. Grcar, M. J. Lijewski, in: P. Wessleing, E. Onate, J. Périaux (Eds.), Proceedings of the European Conference on Computational Fluid Dynamics, Egmond Aan Zee, The Netherlands, 2006, pp. 432:1–19, 5–8 September.

[39] M. Frenklach, H. Wang, M. Goldenberg, G. P. Smith, D. M. Golden, C. T. Bowman, R. K. Hanson, W. C. Gardiner, V. Lissianski, *GRI-Mech—An Optimized Detailed Chemical Reaction Mechanism for Methane Combustion*, Tech. Rep. GRI-95/0058, Gas Research Institute, `http://www.me.berkeley.edu/gri_mech/` (1995).

[40] J. B. Bell, M. S. Day, I. G. Shepherd, M. Johnson, R. K. Cheng, J. F. Grcar, V. E. Beckner, M. J. Lijewski, *Proc. Natl. Acad. Sci. USA* 102 (29) (2005) 10006–10011.

[41] J. B. Bell, M. S. Day, J. F. Grcar, M. J. Lijewski, J. F. Driscoll, S. F. Filatyev, *Proc. Combust. Inst.* 31 (2007) 1299–1307.

[42] R. J. Kee, J. F. Grcar, M. D. Smooke, J. A. Miller, *PREMIX: A Fortran Program for Modeling Steady, Laminar, One-Dimensional Premixed Flames*, Technical Report SAND85-8240, Sandia National Laboratories, Livermore (1983).

[43] A. S. Almgren, J. B. Bell, P. Colella, L. H. Howell, M. L. Welcome, *J. Comput. Phys.* 142 (1998) 1–46.

[44] R. K. Cheng, D. Littlejohn, *Journal of Engineering for Gas Turbines and Power,* in press (2008), also ASME GT2007-27512.

[45] A. J. Aspden, N. Nikiforakis, S. B. Dalziel, J. B. Bell, *Characterising Implicit LES Methods*, *submitted for publication* (2008).

[46] M. Garland, *Quadric-based polygonal surface simplification*, Ph.D. thesis, Carnegie Mellon University (1999).

[47] P.-T. Bremer, V. V. Pascucci, *A Practical Approach to Two-dimensional Scalar Topology*, Mathematics and Visualization, Springer Verlag, Berlin, 2007.

[48] A. Gyulassy, V. Natarajan, V. Pascucci, P.-T. Bremer, B. Hamann, *IEEE Trans. Vis. Comp. Graph.* 12 (4) (2006) 474–484.

[49] D. Laney, P.-T. Bremer, A. Mascarenhas, P. Miller, V. Pascucci, *IEEE Trans. Vis. Comp. Graph.* 13 (1) (2006) 1053–1060.

[50] A. Gyulassy, V. Natarajan, B. Hamann, M. Duchaineau, V. Pascucci, B. E., A. Higginbotham, *IEEE Trans. Vis. Comp. Graph.* 13 (6) (2007) 1432–1439.

[51] P.-T. Bremer, H. Edelsbrunner, B. Hamann, V. Pascucci, *IEEE Transactions on Visualization and Computer Graphics* 10 (4) (2004) 385–396.

[52] J. B. Bell, R. K. Cheng, M. S. Day, I. G. Shepherd, *Proc. Combust. Inst.* 31 (2007) 1309–1317.

[53] J. F. Grcar, J. B. Bell, M. S. Day, *Proc. Combust. Inst.* 32 (in press) (2008) *(Also appears as Lawrence Berkeley National Laboratory Technical Report LBNL-669E).*

Mean Curvature (Normalized by δ_L^{-1})

Case	Mean	Median	SD	Skew	Kurt
Strong	0.267	0.257	0.197	0.124	0.806
Weak	0.274	0.245	0.172	0.6012	1.061
None	0.340	0.316	0.179	0.4024	0.289

Table 1
Properties of the distribution of mean curvature (Normalized by δ_L^{-1})) in Figure 5a.
SD, Skew, and Kurt refer to standard deviation, skewness and kurtosis, respectively.

Gaussian Curvature (Normalized by δ_L^{-2})

Case	Mean	Median	SD	Skew	Kurt
Strong	0.059	0.036	0.103	1.26	4.10
Weak	0.066	0.039	0.100	1.68	5.43
None	0.103	0.067	0.123	1.26	2.52

Table 2
Properties of the distribution of Gaussian curvature normalized by δ_L^{-2}) in Figure 5b. SD, Skew, and Kurt refer to standard deviation, skewness and kurtosis, respectively.

List of Figures

Fig. 1. (a) Mean inflow velocity for the controlled hydrogen-air flame cases studied. The green line indicates the drift of the mean location of the $u' = 0$ flame from the control position (in microns) as the simulation progressed. (b) Typical $T =$1200 K isotherm, colored by local hydrogen consumption rate, ω_{H_2}, for the strong turbulence case. Here, red-colored regions are consuming fuel at over three times the rate of the corresponding flat flame.
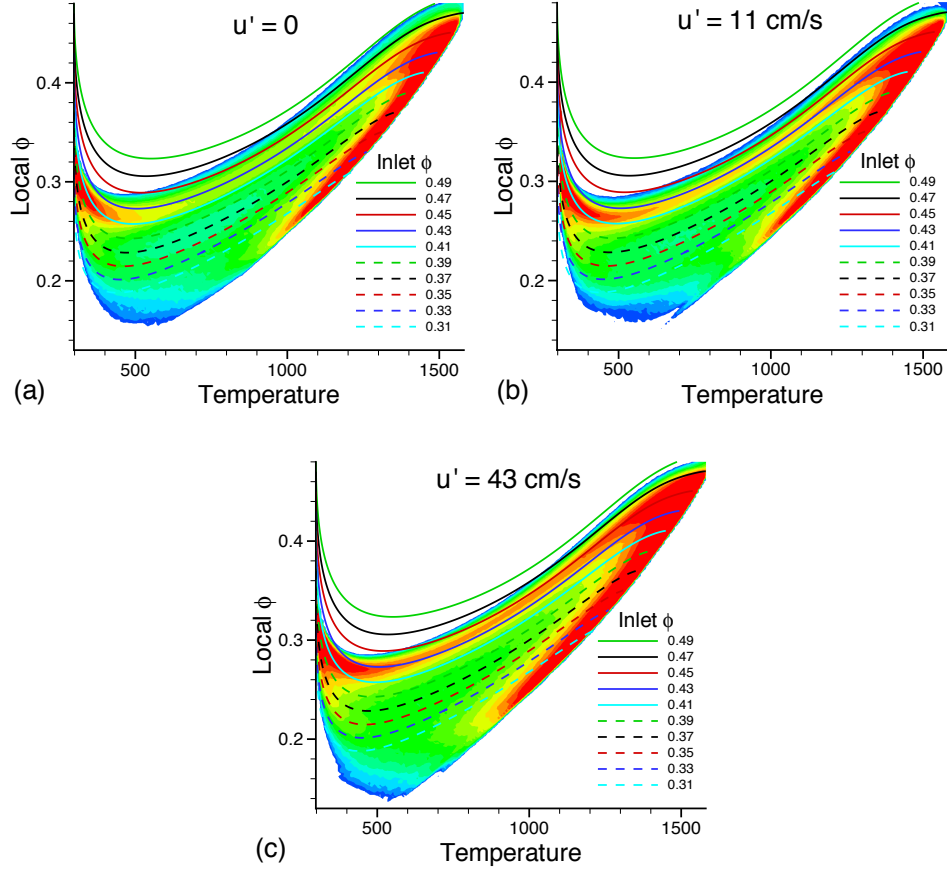
Fig. 2. Log of the joint probability density of local atomic mixture, ϕ^ℓ, with temperature, for a snapshot of each of the (a) $u' = 0$, (b) $u' = 11$ cm/s, and (c) $u' = 43$ cm/s solutions. All cases are overlayed with ϕ^ℓ as a function of T for flat flame solutions at a range of inlet mixtures.
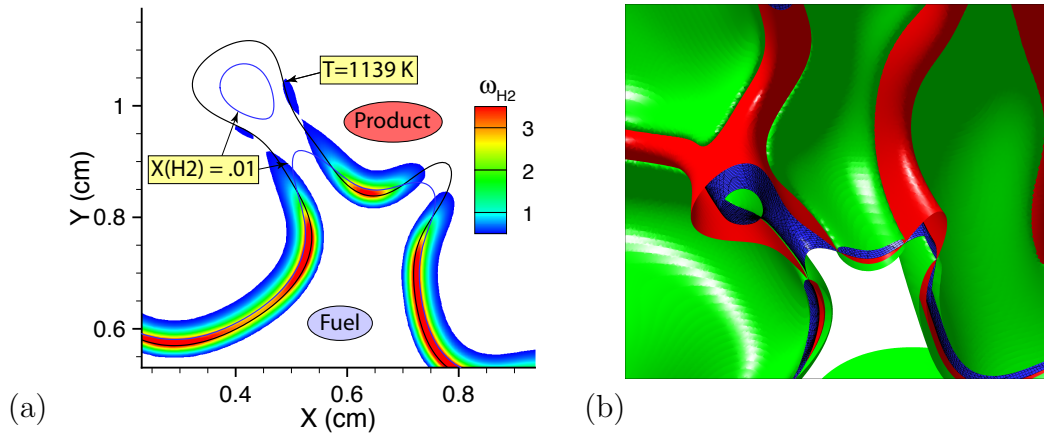
Fig. 3. (a) Typical slice of the instantaneous fuel consumption profile near the flame surface from the $u' = 0$ case; the value is colored on a linear scale, and is normalized by the peak value achieved in the corresponding flat flame solution, ω_{max}. Only the top 98th percentile of fuel consumption is colored. The hydrogen mole fraction and temperature associated with the peak consumption rate are, respectively $X(H_2) = .01$ and $T = 1139$ K. (b) A three-dimensional view of the geometry of the relevant isopleths near the slice shown in (a). Here, the isotherm is colored red, the fuel is blue, and $\omega_{H2} = \omega_{max}$ is green. Within the burning areas, the temperature and fuel gradients are nearly aligned. Outside these regions, these fields are essentially decoupled; the isotherms make particularly large excursions into the products.
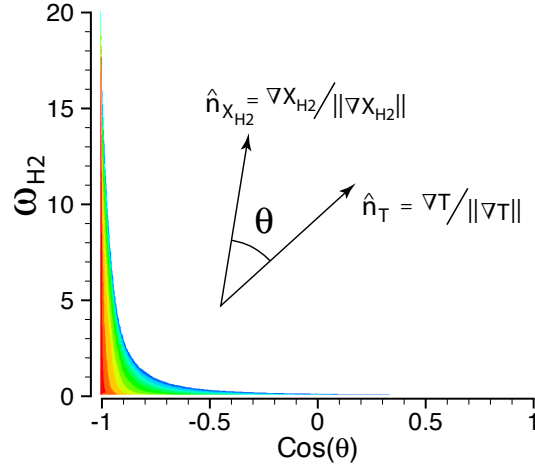
Fig. 4. The log of the moment of the JPDF of $\cos\theta$ vs. fuel consumption rate. θ is the angle between the temperature and fuel gradient vectors. The moment is taken with respect to the consumption rate. Where there is significant fuel consumption the two vectors are predominantly anti-parallel.
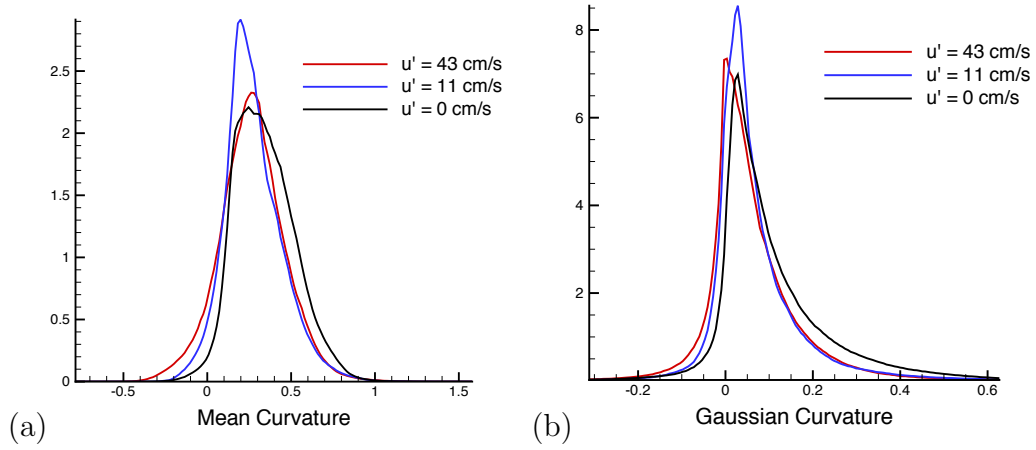
Fig. 5. PDF's of (a) mean curvature (normalized by δ_L), and (b) Gaussian curvature (normalized by δ_L^2) of the flame isotherm, conditioned on burning, for the various levels of turbulence.
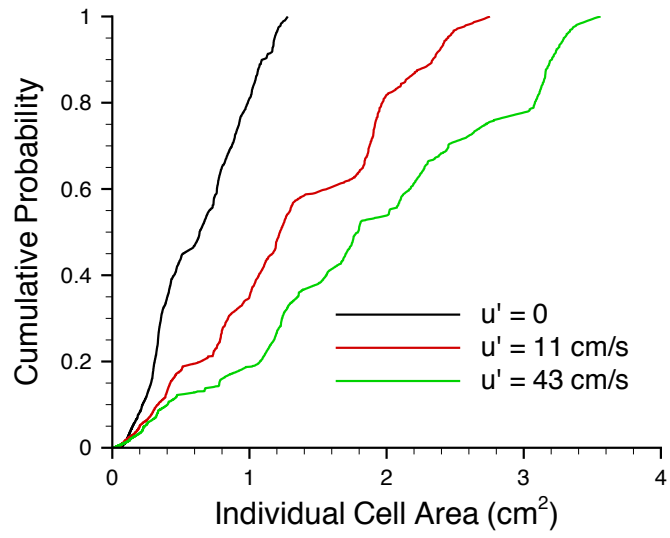
Fig. 6. Cummulative probability distributions of the burning cell structures, showing that higher turbulence generates larger cells and an increased flame surface area.
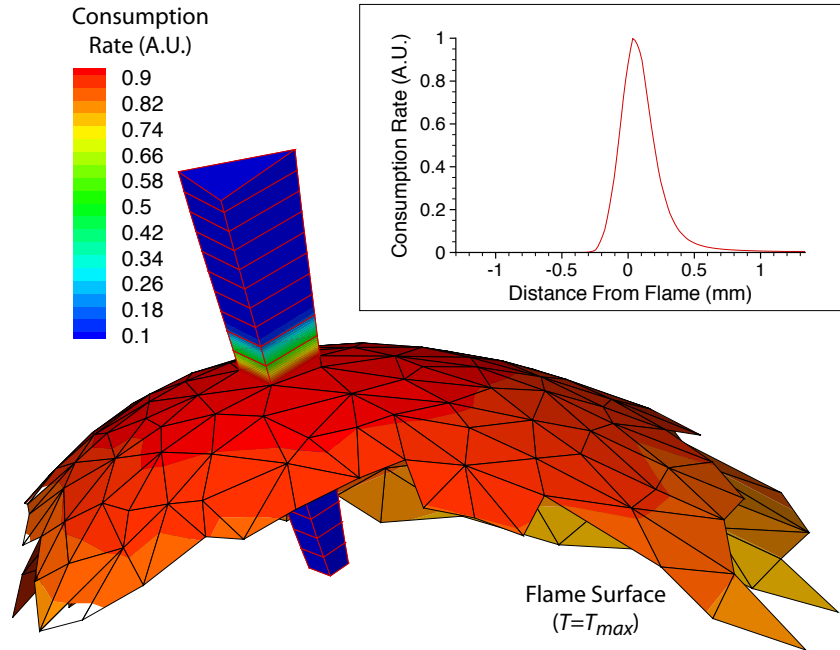
Fig. 7. Prism-shaped volume, Ω, constructed using curves locally normal to the temperature isotherms (both the flame and Ω are colored by a typical profile of fuel consumption rate, ω_{H2}). The inset plot shows the variation of ω_{H2} normal to the flame surface. Ω discretizes the flame volume, and the integral curves of T that bound Ω define a set of local flame coordinates.
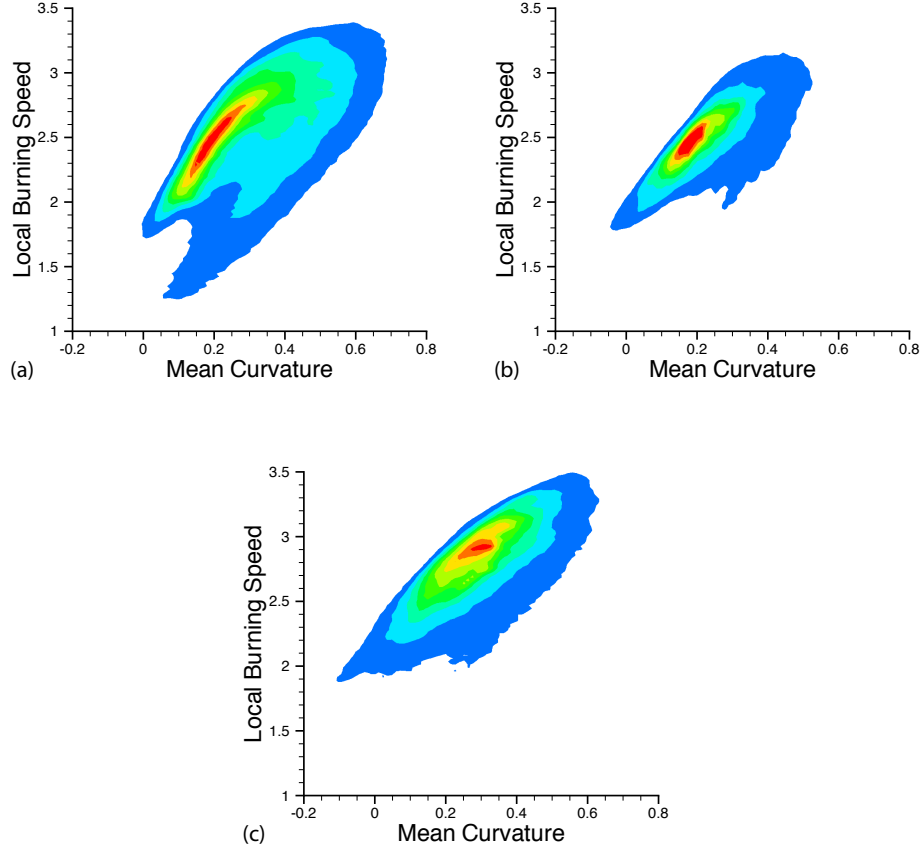
Fig. 8. Joint PDFs of normalized mean curvature ($K \cdot \delta_L$) vs. normalized burning speed (S_c^{ℓ}/s_L) for the (a) u'=0, (b) u'=11 cm/s, and (c) u'=43 cm/s cases. The color bands represent the moment of the area-weighted probability density with respect to the consumption rate, scaled logarithmically. Where the flame is burning significantly, the local consumption speed exhibits a strong positive correlation with K.
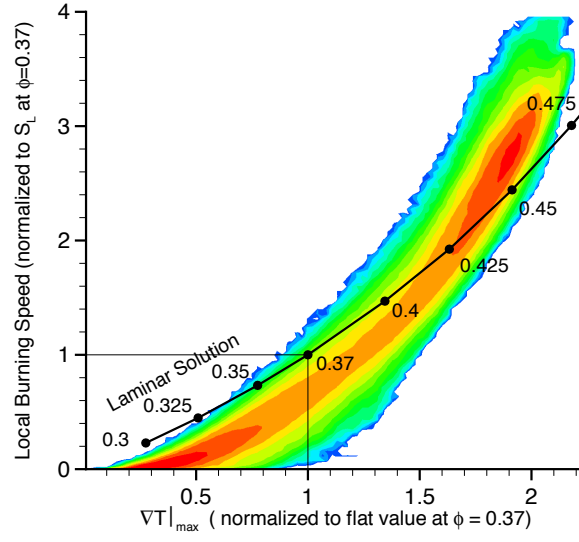
Fig. 9. Joint PDF of local burning speed and peak thermal gradient measured locally normal to the flame for the strong case, scaled logarithmically. Both plotted quantities are normalized to the respective values obtained from the flat flame idealization.
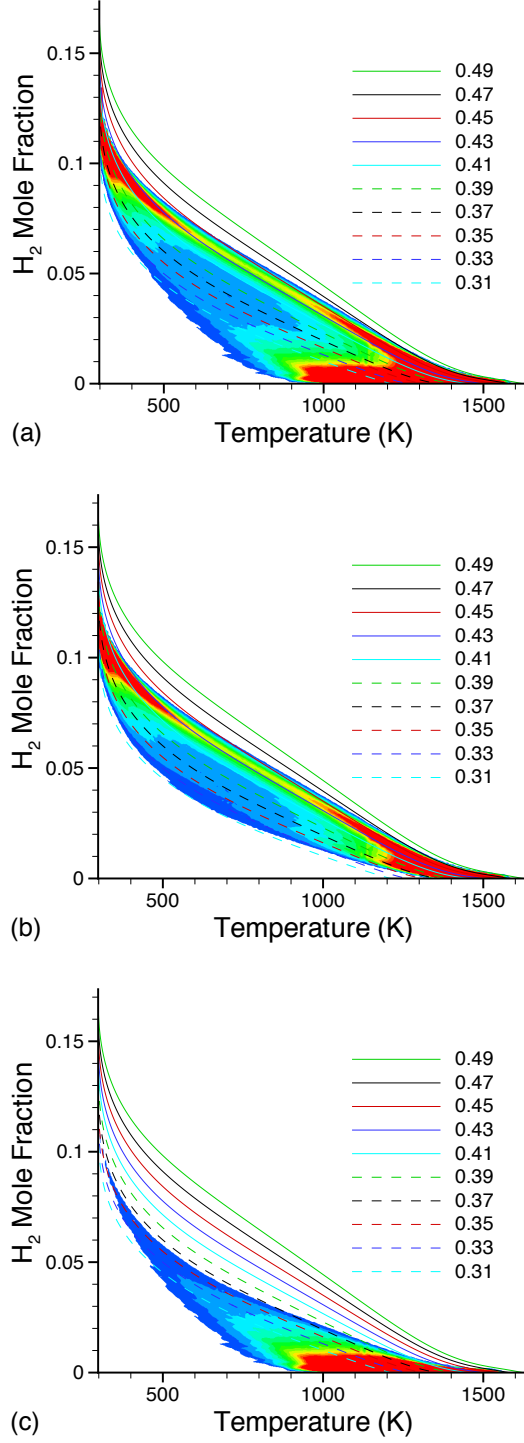
Fig. 10. Joint PDF of $X(H_2)$ versus T in neighborhood of the unconditioned flame. (a) shows the full JPDF; (b) and (c) show the portion of data for which $X(H_2)$ is greater than or less than 0.0104 on the $T = 1139$ isotherm, respectively. This criterion roughly separates the data into components that are burning more or less intensely than a $\phi = 0.37$ flat laminar flame.
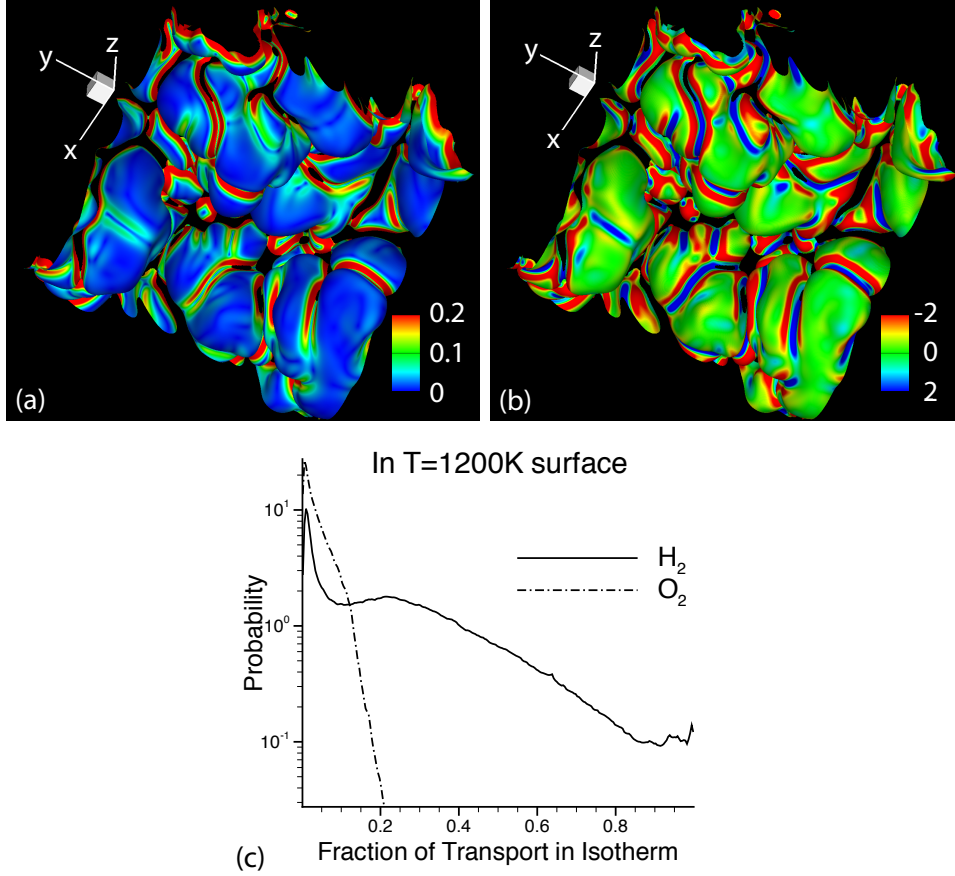
35

Fig. 11. A typical flame ($T = T_{\omega-max}$) isotherm from the strong turbulence case, colored by (a) the fraction of local H_2 diffusive flow in the $T = T_{\omega-max}$ isotherm, and (b) the divergence (in $1/s$) of the H_2 diffusive flow velocity in the $T = T_{\omega-max}$ isotherm, indicating that between cellular burning structures, there is a local sink of H_2 molecules, and a corresponding source along the edges of the cells. (c) Distribution of the in-flame transport for H_2 and O_2. For clarity, only the region of the flame surface where $\omega_{H_2} < 0.35\omega_{max}$ is shown. Shapshots at different times, and for the other two cases appear qualitatively similar, and are not shown.